

# Performance of Perovskite CsPbBr<sub>3</sub> Single Crystal Detector for Gamma-Ray Detection

Lei Pan<sup>1</sup>, Yuanxiang Feng, Praneeth Kandlakunta<sup>2</sup>, Jinsong Huang, and Lei R. Cao<sup>1</sup>

**Abstract**—The lead (Pb) halide perovskites show great potential in X- and gamma-ray detection with a high attenuation coefficient, wide bandgap energy, and large mobility-lifetime ( $\mu\tau$ ) product. Among them, the all-inorganic cesium lead bromide (CsPbBr<sub>3</sub>) perovskite offers advantages over the organic-inorganic perovskites due to its structural stability. We report gamma-ray detectors made of solution-grown perovskite CsPbBr<sub>3</sub> single crystal that is able to produce energy spectra from cesium-137 (<sup>137</sup>Cs), cobalt-57 (<sup>57</sup>Co), and americium-241 (<sup>241</sup>Am) sources with a full-width-half-maximum of 5.5% at 662 keV, 13.1% at 122 keV, and 28.3% at 59.5 keV, respectively. The difference between electron and hole transport properties of CsPbBr<sub>3</sub> is demonstrated to have a significant effect on detector spectral performance as evidenced by primarily hole-induced as well as primarily electron-induced gamma-ray spectra. Electron-hole averaged  $\mu\tau$  product is evaluated to be  $4.0 \times 10^{-4} \text{ cm}^2\text{V}^{-1}$  by fitting the Hecht equation. A digital pulse processing (DPP) algorithm is also developed to process preamplifier pulses with potentially long transit time (on the order of tens of microseconds) in perovskite detectors, which ensures the elimination of ballistic deficit in subsequent pulse processing for distortion-free energy spectra reconstruction.

**Index Terms**—CsPbBr<sub>3</sub>, digital pulse processing (DPP), electron/hole transport, energy spectrum, gamma-ray detectors, perovskite.

## I. INTRODUCTION

ROOM temperature semiconductor radiation detectors are highly preferred for broad applications in numerous fields of defense, industry, medical imaging, and research [1]–[3]. Such applications demand the characteristic gamma-ray ( $\gamma$ -ray) energy spectra of different radionuclides to be resolved with performance as good as, if not better than, a high purity germanium detector. An ideal, well-performing  $\gamma$ -ray detector with high intrinsic efficiency and high-energy resolution for room temperature operation requires materials of high  $\gamma$ -ray attenuation coefficient, wide bandgap energy,

and large mobility-lifetime ( $\mu\tau$ ) product. The cadmium-zinc-telluride (CdZnTe or CZT) detector has witnessed great development over the last few decades, achieving a resolution down to 0.48% full-width-half-maximum (FWHM) at 662 keV [4]. Nevertheless, its growth issues associated with high fabrication cost [5]–[7] continue to drive the search for alternative radiation detection materials featuring large volume and low-cost growth methods.

Lead (Pb) halide perovskites with formula APbX<sub>3</sub> [where A<sup>+</sup> = Cesium (Cs) or methylammonium (MA or CH<sub>3</sub>NH<sub>3</sub>) and X<sup>−</sup> = chlorine (Cl), bromine (Br) or iodine (I)] are highly attractive as room temperature  $\gamma$ -ray detectors with an estimated raw material cost of \$0.3–3 cm<sup>−3</sup> after scaling up [8], [9] high  $\gamma$ -ray attenuation coefficient due to the presence of Pb, low charge trap density and defect tolerance [9]–[13]; wide bandgap energy [8], [9], [14]; and hole-dominated  $\mu\tau$  product as high as  $1.8 \times 10^{-2} \text{ cm}^2\text{V}^{-1}$  evaluated using a light source or X-rays [8], [9], [15]. It is reported that perovskite materials exhibit much more tolerance to radiation-induced damage than many other radiation detection semiconductors [16], though it is still not clear whether the induced defects would impact the radiation detectors which operate under a much higher electric field than that in solar cells. Organic-Inorganic Halide Perovskites (OIHPs) with CH<sub>3</sub>NH<sub>3</sub> grown into a crystal in the solution method have been fabricated as  $\gamma$ -ray detectors. A dopant-compensated variation CH<sub>3</sub>NH<sub>3</sub>PbBr<sub>3−x</sub>Cl<sub>x</sub> for improving resistivity has been reported with a full energy peak resolution of 6.5% at 662 keV for cesium-137 (<sup>137</sup>Cs) [8]. A Schottky-type CH<sub>3</sub>NH<sub>3</sub>PbI<sub>3</sub>  $\gamma$ -ray detector has achieved 6.8% resolution at 122 keV for cobalt-57 (<sup>57</sup>Co) and 12% resolution at 59.5 keV for americium-241 (<sup>241</sup>Am) [17]. Although OIHPs achieve such a remarkable  $\gamma$ -ray spectral performance, their instability due to the presence of organic cation [18]–[20] under heat or moisture remains a concern unfavorable for long-term usage. On the contrary, upon replacing organic cation by its inorganic counterpart, all-inorganic perovskite CsPbBr<sub>3</sub> shows superior long-term stability chemically and mechanically, while maintaining desirable electric and photovoltaic properties [13], [21]–[24]. CsPbBr<sub>3</sub> single crystals have been grown, characterized, and shown to perform well in a photoresponse test [14], [21], [22], [24], [25]. A CsPbBr<sub>3</sub> detector is reported to be able to detect the 59.5 keV photopeak of <sup>241</sup>Am source when cooled to −53 °C [21]. Another work reported that CsPbBr<sub>3</sub> detectors are able to acquire <sup>57</sup>Co  $\gamma$ -ray energy spectrum with 3.9% FWHM at 122 keV and <sup>137</sup>Cs

Manuscript received September 27, 2019; accepted January 2, 2020. Date of publication January 7, 2020; date of current version February 13, 2020. This work was supported by the Department of the Defense, Defense Threat Reduction Agency, under Grant HDTRA1170054.

Lei Pan, Praneeth Kandlakunta, and Lei R. Cao are with the Nuclear Engineering Program, Department of Mechanical and Aerospace Engineering, The Ohio State University, Columbus, OH 43210 USA (e-mail: pan.707@osu.edu; kandlakunta.1@osu.edu; cao.152@osu.edu).

Yuanxiang Feng and Jinsong Huang are with the Department of Applied Physical Sciences, The University of North Carolina at Chapel Hill, Chapel Hill, NC 27514 USA (e-mail: bjzhong@live.unc.edu; jhuang@unc.edu).

Color versions of one or more of the figures in this article are available online at <http://ieeexplore.ieee.org>.

Digital Object Identifier 10.1109/TNS.2020.2964306

$\gamma$ -ray energy spectrum with 3.8% FWHM at 662 keV at room temperature [26]. Despite all early achievements, there has been a lack of consistent report of such detectors'  $\gamma$ -ray spectroscopic performance, and an analysis of energy spectral performance in the context of conventional analog-based nuclear instruments and the comparison to digital-based methods, i.e., digital pulse processing (DPP).

A typical analog spectroscopy system acquires  $\gamma$ -ray energy spectra with a preamplifier, a shaping amplifier, and an analog-to-digital converter (ADC) embedded multi-channel analyzer (MCA), whereas the digital-based method applies digital filters to digitized waveform signals immediately after the preamplifier stage, eliminating the use of the shaping amplifier and pulse height sorting by MCA [27]. In the applications where the detector's current transit time is longer than the shaping amplifier's time constant, DPP shows more flexibility as opposed to using the shaping amplifier that may cause spectrum distortion due to ballistic deficit. The charge carrier velocity/mobility is a material-dependent property that is a more useful characteristic compared to charge carrier transit times which vary with detector thickness. Nevertheless, from a practical standpoint of a detector at a given thickness, transit time is the parameter to be taken into consideration and its impact on spectral performance must be well informed. Various current transit times in perovskite detectors have been reported, including those in  $\text{CH}_3\text{NH}_3\text{PbBr}_3$  detectors which are on the order of tens of microseconds under an electric field of  $\sim 800$  V/cm (hole drift velocity of  $\sim 10^4$  cm/s at a detector thickness of 1–3 mm) [28]. This current transit time is much longer than that in a Si detector (tens of nanoseconds, i.e., an electron drift velocity from  $\sim 3 \times 10^6$  to  $5 \times 10^6$  cm/s at detector thicknesses from  $\sim 100$   $\mu\text{m}$  to 2 mm) and CZT detector (hundreds of nanoseconds, i.e., an electron drift velocity from  $\sim 1 \times 10^6$  to  $2 \times 10^6$  cm/s at detector thicknesses from  $\sim 1$  to 10 mm) [29]. In comparison, the current transit time of a  $\text{CsPbBr}_3$  detector is reported to be several microseconds under a range of electric field  $\sim 400$ – $800$  V/cm [30]. The long current transit time of perovskite detectors could cause a ballistic deficit and subsequent  $\gamma$ -ray energy spectra distortion if the choice of preamplifier and shaping amplifier time constants is not matched to detector's current transit time [28]. On the contrary, the versatility of DPP circumvents the traditional pulse-shaping process, thereby eliminating this issue.

In this work, we report the acquisition and analysis of  $\gamma$ -ray spectra from  $\text{CsPbBr}_3$  detectors. Gamma-ray spectra with FWHM of 5.5% at 662 keV for  $^{137}\text{Cs}$ , 13.1% at 122 keV for  $^{57}\text{Co}$ , and 28.3% at 59.5 keV for  $^{241}\text{Am}$  are acquired by the  $\text{CsPbBr}_3$  detector with energy linearity  $R^2$  nearly equal to unity. The effect of unbalanced electron and hole transport properties of  $\text{CsPbBr}_3$  on  $\gamma$ -ray energy spectra is evaluated. We have also developed a DPP algorithm to process the preamplifier pulses from  $\text{CsPbBr}_3$  detectors with a range of transit times (several to tens of microseconds) after digitization by an oscilloscope.

## II. GAMMA-RAY SPECTRA PERFORMANCE

Several detectors (labeled as detector I, II, and III, respectively, with their physical dimensions) were tested and the best

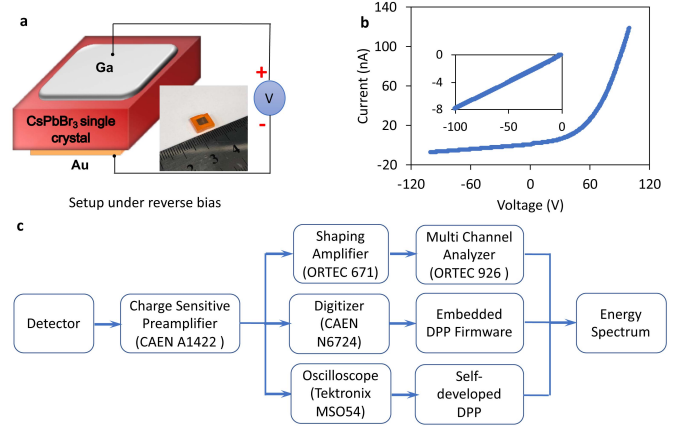


Fig. 1.  $\text{CsPbBr}_3$  detector. (a)  $\text{CsPbBr}_3$  detector I ( $2.53 \times 7.08 \times 8.29 \text{ mm}^3$ ). Inset shows a real photograph of the device with Au contact. (b)  $I - V$  curve of  $\text{CsPbBr}_3$  detector I. (c) Three experimental setups used for data acquisition, i.e., analog, digitizer, and oscilloscope in waveform mode as our three gamma spectroscopy systems.

spectral performance produced by detector I is presented and analyzed in this section. The gallium (Ga)/ $\text{CsPbBr}_3$ /gold (Au) structure has been selected to produce the best achievable  $\gamma$ -ray energy spectra [see Fig. 1(a)]. The  $\text{CsPbBr}_3$  crystals were synthesized by the solution growth method, for example, 3.523-g  $\text{PbBr}_2$  and 1.021-g  $\text{CsBr}$  were dissolved into 5.5-mL Dimethyl sulfoxide (DMSO) at  $100^\circ\text{C}$  for one growth. The solution was then filtered with a  $0.2 \mu\text{m}$  polytetrafluoroethylene (PTFE) filter, and heated at  $115^\circ\text{C}$  for 48 to 72 h to grow large crystals. The devices were finished by evaporating a 50-nm Au electrode on one side of the crystal and applying the Ga electrode on the other side. The image of the Au side of the detector is shown in Fig. 1(a). The as-grown  $\text{CsPbBr}_3$  single crystals are p-type, with which Ga (low work function metal) forms the Schottky contact while Au (high work function metal) forms Ohmic contact. The  $I - V$  curve measured with KEITHLEY 4200A-SCS<sup>1</sup> [see Fig. 1(b)] verifies the Schottky and Ohmic behavior of Ga and Au contacts, respectively. The Ga or Au electrode area is  $4.5 \times 4.5 \text{ mm}^2$ , centered on the  $7.08 \text{ mm} \times 8.29 \text{ mm}$  detector surface, which results in an effective detection volume of  $2.53 \times 4.5 \times 4.5 \text{ mm}^3$ . Three different experimental setups used in this work for  $\gamma$ -ray spectroscopy are shown in Fig. 1(c). The analog system has a charge-sensitive preamplifier (CAEN MOD A1422 F3, GAIN = 90 mV/MeV, decay time = 50  $\mu\text{s}$ ) connected subsequently to a shaping amplifier (ORTEC 671, maximum shaping constant 10  $\mu\text{s}$ ) and an MCA (ORTEC 926) that allows  $\gamma$ -ray energy spectra acquisition through commercial spectroscopy software. Alternatively, a digitizer (CAEN N6724) that employs vendor-supplied DPP firmware and an oscilloscope (Tektronix MSO54) working under the triggered waveform capture mode with self-developed DPP were also used.

The  $\gamma$ -ray spectra from  $^{137}\text{Cs}$  (5.29  $\mu\text{Ci}$ ),  $^{57}\text{Co}$  (0.05  $\mu\text{Ci}$ ), and  $^{241}\text{Am}$  (1  $\mu\text{Ci}$ ) were acquired with an analog system

<sup>1</sup>Certain commercial products are identified in this article in order to specify the experimental procedures in adequate detail. This identification does not imply recommendation or endorsement by the authors nor does it imply that the products identified are necessarily the best available for the purpose.

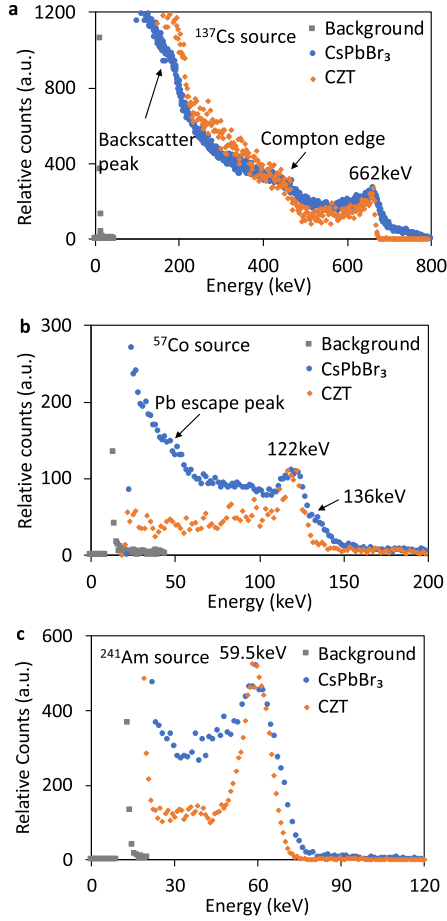


Fig. 2. Comparison of  $\gamma$ -ray energy spectra of CsPbBr<sub>3</sub> detector I and a commercial CZT detector. (a) <sup>137</sup>Cs. (b) <sup>57</sup>Co. (c) <sup>241</sup>Am  $\gamma$ -ray energy spectra acquired with CsPbBr<sub>3</sub> detector I ( $2.53 \times 7.08 \times 8.29 \text{ mm}^3$ ) and CZT ( $5 \times 5 \times 4 \text{ mm}^3$ ) detector under same experimental conditions (bias 500 V, shaping time 10  $\mu$ s).

(see Fig. 2). The energy resolution of a CsPbBr<sub>3</sub> detector indicated by FWHM is 5.5% at 662 keV in Fig. 2(a), 13.1% at 122 keV in Fig. 2(b), and 28.3% at 59.5 keV in Fig. 2(c), respectively. The spectra from the same sources were also acquired with a commercial spectrometer grade CZT detector ( $5 \times 5 \times 4 \text{ mm}^3$ , Kromek) for comparison. The CZT detector was intentionally purchased with its size as close as possible to the effective detection volume of the CsPbBr<sub>3</sub> detector ( $2.53 \times 4.5 \times 4.5 \text{ mm}^3$ ). The CZT detector is also made with the same parallel plate electrode structure as the CsPbBr<sub>3</sub> detector, which is known to yield a low Peak-to-Compton ratio and low energy tailing effect [31], [32]. The CsPbBr<sub>3</sub> spectra are remarkably similar to the spectra of the CZT detector using a simple planar structure, implying that the resolution limiting factors of CZT, i.e., different electron/hole transport property and size effects, also apply to the CsPbBr<sub>3</sub> detector. It further suggests that the resolution of the CsPbBr<sub>3</sub> detector could be improved if single polarity charge sensing (e.g., pixelated electrode) can be applied, which has significantly improved the resolution of the CZT detector [32]. It is also noted that the high energy end of the photopeak in CsPbBr<sub>3</sub> spectra has a longer tail than that in CZT spectra. This may be viewed as a manifestation of poor CsPbBr<sub>3</sub> spectral resolution resulting

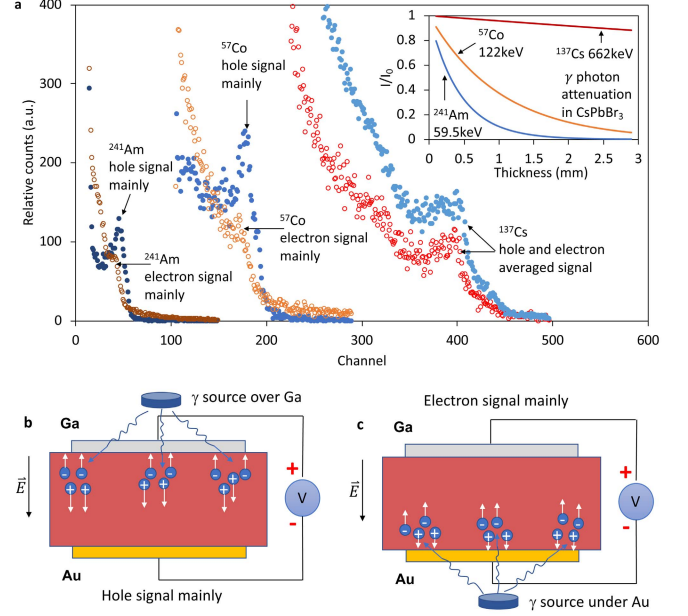


Fig. 3. Analysis of electron and hole transport properties at spectroscopy level. (a) <sup>137</sup>Cs, <sup>57</sup>Co, <sup>241</sup>Am  $\gamma$ -ray energy spectra acquired under different source-to-detector configurations for comparison of the effects of electron and hole transport properties on spectral performance. All spectra are acquired by CsPbBr<sub>3</sub> detector I at 500 V with a shaping time of 10  $\mu$ s. Shown in the inset of Fig. 3(a) is the  $\gamma$ -ray photon attenuation in CsPbBr<sub>3</sub> at different energies. (b) Setup for acquisition of spectrum induced mainly by hole transport signal. (c) Setup for acquisition of spectrum induced mainly by electron transport signal.

from noise and the higher statistical variance in charge carrier generation due to the higher bandgap of CsPbBr<sub>3</sub>. Detector surface leakage current certainly plays a role in photopeak broadening, which may be reduced by surface polishing and passivation.

#### A. Unbalanced Electron and Hole Transport

Contrary to CZT where the hole  $\mu\tau$  product is lower than that of the electron (thus leading to low energy tailing in the spectrum), previous work has shown that CsPbBr<sub>3</sub> single crystal has a lower electron  $\mu\tau$  product [ $(\mu\tau)_e = 8.77 \times 10^{-4} \text{ cm}^2/\text{V}$ ,  $(\mu\tau)_h = 1.34 \times 10^{-3} \text{ cm}^2/\text{V}$  [26];  $(\mu\tau)_e = 4.5 \times 10^{-4} \text{ cm}^2/\text{V}$ ,  $(\mu\tau)_h = 9.5 \times 10^{-4} \text{ cm}^2/\text{V}$  [30]], which leads to asymmetric Gaussian shape for full-energy  $\gamma$ -ray peaks as well. To observe the energy resolution degradation due to the unbalanced electron and hole transport properties, we compared the spectral performance attributed to electron or hole transport by switching the  $\gamma$ -ray source position relative to the detector. Gamma-ray photons with different penetration depths in CsPbBr<sub>3</sub> were used to acquire spectra affected differently by electrons and hole transport. The fraction of incident photon intensity at a thickness “ $x$ ” inside CsPbBr<sub>3</sub> is calculated using (1) and shown in Fig. 3(a) (inset) for a semiquantitative analysis in understanding the penetration depth of photons of different energies

$$I/I_0 = e^{-\frac{\mu}{\rho}(\rho x)}, \quad \mu/\rho = \sum_i w_i(\mu/\rho)_i. \quad (1)$$

In our calculation,  $I_0$  is the incident gamma photon intensity,  $I$  is the gamma photon intensity at a thickness “ $x$ ,”  $\mu/\rho$



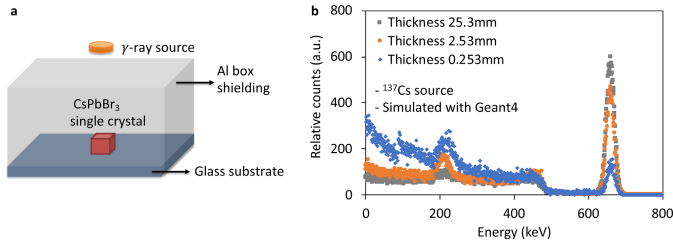


Fig. 4. Effect of detector size on the  $\gamma$ -ray spectrum observed using Geant4 simulations. (a) Geant4 simulation model for  $^{137}\text{Cs}$   $\gamma$ -ray energy spectrum of  $\text{CsPbBr}_3$  detector. (b)  $^{137}\text{Cs}$   $\gamma$ -ray energy spectra of  $\text{CsPbBr}_3$  detector with different thicknesses simulated in Geant4.

is the mass attenuation coefficient of  $\text{CsPbBr}_3$ , and  $w_i$  and  $(\mu/\rho)_i$  are the weight fraction and mass attenuation coefficient, respectively, of the  $i$ th atomic constituent.

Given the limited penetration depth of 59.5 keV  $\gamma$ -ray photons from  $^{241}\text{Am}$  source, i.e.,  $<10\%$  transmission over the first 1-mm thickness, the spectrum from  $^{241}\text{Am}$  source placed over Ga electrode or under Au electrode could be treated as mainly induced by hole transport [see Fig. 3(b)] or mainly induced by electron transport [see Fig. 3(c)], respectively. The spectrum mainly with hole transport clearly presents a stronger and more symmetric 59.5-keV full energy peak compared to that of mainly electron transport [see Fig. 3(a)]. The same phenomenon is still observable with 122-keV full energy peak from the  $^{57}\text{Co}$  source since its low penetration depth still produces a concentration gradient of electron-hole pairs along the thickness of the  $\text{CsPbBr}_3$  detector [see Fig. 3(a)]. Due to a greater penetration depth of  $^{137}\text{Cs}$   $\gamma$ -ray photons, such effect becomes negligible now that the charge carriers are generated uniformly inside the detector volume, leading to a similar spectrum, regardless of the source-detector configuration [see Fig. 3(a)]. In conclusion, significant difference between spectra attributed mainly to hole or electron transport is observed for  $\text{CsPbBr}_3$  detector under  $\gamma$  rays. It is recognized that an alpha source could produce a more distinguishable difference in spectral performance due to single carrier transport. However, the thick Ga electrode prevented us from using alpha particles in our devices. Furthermore, the transitional features of spectral performance under  $\gamma$  rays of varying energies present more interesting insights into the effects of electron and hole  $\mu\tau$  of  $\text{CsPbBr}_3$  on gamma spectroscopy performance. Similar to the CZT detector, one type of charge carrier cannot be collected as effectively as the other in  $\text{CsPbBr}_3$ , which would lead to energy resolution degradation when a simple parallel electrode structure is being used. Further resolution improvement could be achieved by employing pixelated electrode to mitigate the impact of an inefficient collection of one type of charge carrier [32]. It is also shown that the arrangement of the source-detector position plays an important role in spectral performance for low energy  $\gamma$ -ray photons, at which the difference in electron and hole transport properties has a bigger effect.

### B. Size Effect

Monte Carlo simulations were performed in Geant4 [33] using the source-detector configuration shown in Fig. 4(a) to

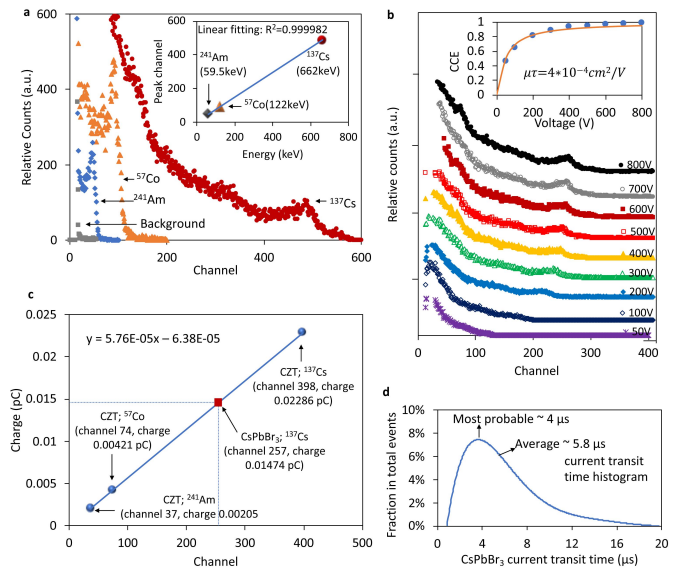


Fig. 5. Energy linearity and  $\mu\tau$  evaluation. (a)  $^{137}\text{Cs}$ ,  $^{57}\text{Co}$ , and  $^{241}\text{Am}$   $\gamma$ -ray energy spectra acquired separately with  $\text{CsPbBr}_3$  detector I under the same experimental conditions, i.e., 500-V bias, 10- $\mu\text{s}$  shaping time. Shown in the inset of Fig. 5(a) is the linear fit of photopeak channel versus photopeak energy. (b)  $^{137}\text{Cs}$   $\gamma$ -ray energy spectra of  $\text{CsPbBr}_3$  detector I at different bias voltages with shaping constant of 10  $\mu\text{s}$  for all acquisition. Inset is Hecht equation fitting for  $\mu\tau$  evaluation. (c) Charge collection calibration with a CZT detector. Theoretical total collected charge for  $^{137}\text{Cs}$ ,  $^{57}\text{Co}$ , and  $^{241}\text{Am}$  sources calculated using CZT electron-hole pair creation energy (assuming full charge collection of CZT) versus saturation channel corresponding to full charge collection of CZT detector. Instrument for CZT detector spectra acquisition was exactly the same as  $\text{CsPbBr}_3$  detector spectra acquisition in Fig. 5(b). (d) Histogram of the current transit time of  $\text{CsPbBr}_3$  detector I under 500 V with  $^{137}\text{Cs}$   $\gamma$  source.

corroborate the effect of size on the peak-to-Compton ratio of the spectra [see Fig. 4(b)]. Three  $^{137}\text{Cs}$   $\gamma$ -ray energy spectra of  $\text{CsPbBr}_3$  detector were simulated with original effective dimensions of  $2.53 \times 4.5 \times 4.5 \text{ mm}^3$  of detector I, the tenth, and the tenfold of its original thickness, respectively. Reduction of detector thickness from 25.3 to 0.253 mm is in favor of  $\gamma$ -ray photons escaping after Compton scattering, which leads to high Compton continuum and hence low peak-to-Compton ratio.

### C. Energy Linearity and Mobility-Lifetime ( $\mu\tau$ ) Product

The plot of the peak centroid channel versus peak energy from  $^{137}\text{Cs}$ ,  $^{57}\text{Co}$ , and  $^{241}\text{Am}$   $\gamma$ -ray energy spectra of  $\text{CsPbBr}_3$  detector I [see Fig. 5(a)] indicates good energy linearity over the measured energy range. A series of  $^{137}\text{Cs}$   $\gamma$ -ray energy spectra were acquired with detector I [see Fig. 5(b)]. The full energy peak shifts to higher channels and becomes more prominent at higher biasing voltages.

Charge collection efficiency (CCE) is estimated with the help of charge versus channel system calibration using the same commercial CZT detector presented in Fig. 2. The instrument is calibrated by fitting the saturated photopeak channels of varying  $\gamma$ -ray energies acquired by CZT to the corresponding theoretically generated charge calculated using electron-hole pair creation energy ( $w$ -value) 4.64 eV of CZT [29], which yields the relationship of collected charge

to the channel numbers [see Fig. 5(c)]. The collected charge,  $Q$ , of CsPbBr<sub>3</sub> detector corresponding to a photopeak is then obtained from this relationship, knowing the measured photopeak channel number. The theoretically generated charge in CsPbBr<sub>3</sub> detector by one 662 keV  $\gamma$  photon is calculated as  $Q_0 = 662 \text{ keV} \times e/W$ , where “ $e$ ” is the elementary charge and  $W$  is the average electron–hole pair creation energy ( $W$ -value) evaluated through an empirical equation,  $W = 2.73 E_g + 0.55$  [34] ( $E_g$  (bandgap energy) = 2.23 eV for CsPbBr<sub>3</sub>[13]). The CCE is then estimated by taking the ratio of experimentally measured collected charge to the theoretically generated charge, which is 92.3% for the tested CsPbBr<sub>3</sub> detector at 800 V with <sup>137</sup>Cs source. The incomplete charge collection may be attributed to the inefficient electron collection. Obviously, the accuracy of CCE estimation depends on the accuracy of the  $W$ -value, which highlights the importance of evaluating the  $W$ -value of CsPbBr<sub>3</sub> detectors.

Hecht equation fitting is used to estimate the  $\mu\tau$  product. Ideally and more accurately, an alpha source should be used for the  $\mu\tau$  estimation to produce a near-surface charge by short-ranged alpha particles that satisfy the requirement of single carrier Hecht equation [30]. However, the CsPbBr<sub>3</sub> detector with a thick Ga electrode ( $\sim 1\text{--}2$  mm thick) prevented us from using an alpha particle source. As a substitute, the <sup>137</sup>Cs  $\gamma$ -ray energy spectra were used for Hecht equation fitting [see Fig. 5(b)]. Since the 662-keV  $\gamma$ -ray photons of <sup>137</sup>Cs are able to fully penetrate the volume of CsPbBr<sub>3</sub> detector [see Fig. 3(a)], the induced charge is contributed by both electron and hole transport. In this case, a  $\mu\tau$  that effectively averages the electron and hole  $\mu\tau$  values can be estimated by (2) [35]

$$\text{CCE} = \frac{V\mu\tau}{d\langle x \rangle} (1 - e^{-\frac{\langle x \rangle d}{V\mu\tau}}) \quad (2)$$

where  $V$  is the applied bias voltage,  $d$  is the detector thickness,  $\langle x \rangle$  is the estimated average distance that charge carrier drifts to reach the collecting electrodes. Admittedly, the averaged  $\mu\tau$  estimated by (2) could have an uncertainty range as large as a factor of 2, yet it presents an acceptable level of estimation when an alpha source is not applicable [35]. The estimated  $\mu\tau$  is  $4.0 \times 10^{-4} \text{ cm}^2/\text{V}$  with  $\langle x \rangle = d/2$ , which lies at the same level with the reported hole and electron  $\mu\tau$  product values,  $(\mu\tau)_e = 4.5 \times 10^{-4} \text{ cm}^2/\text{V}$ ,  $(\mu\tau)_h = 9.5 \times 10^{-4} \text{ cm}^2/\text{V}$  [30].

A histogram of the current transit time ( $t_r$ ) [see Fig. 5(d)] shows the most probable and average transit time at 500 V. Average transit time of  $5.8 \mu\text{s}$  is used to estimate the charge carrier mobility with equation  $t_r = d^2/(\mu \times V)$  ( $d$  is the detector thickness,  $\mu$  is the charge carrier mobility, and  $V$  is the applied bias voltage). We estimated the mobility to be  $\mu = d^2/(t_r \times V) = 0.253^2 \text{ cm}^2/(5.8 \mu\text{s} \times 500 \text{ V}) = 22 \text{ cm}^2\text{V}^{-1}\text{s}^{-1}$  that can also be considered as electron–hole averaged mobility.

### III. DIGITAL PULSE PROCESSING

#### A. Perovskite Detector Current Transit Time

As reported, the CsPbBr<sub>3</sub> and CH<sub>3</sub>NH<sub>3</sub>PbBr<sub>3</sub> detectors have current transit times from several to tens of microseconds [28], [30]. We also observed CsPbBr<sub>3</sub> detectors that generate current transit time on the order of microseconds or

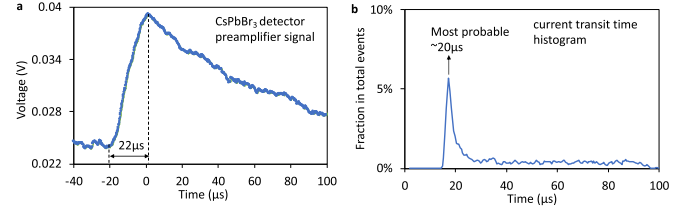


Fig. 6. Voltage pulse and transit times of CsPbBr<sub>3</sub> detector II ( $2.3 \times 5.54 \times 6.21 \text{ mm}^3$ ). (a) Pre-amplifier waveform signal of CsPbBr<sub>3</sub> detector II at 50 V with <sup>137</sup>Cs source. (b) Histogram of current transit time of CsPbBr<sub>3</sub> detector II at 50 V with <sup>137</sup>Cs source.

even tens of microseconds. The preamplifier voltage pulse and transit times of CsPbBr<sub>3</sub> detector II ( $2.3 \times 5.54 \times 6.21 \text{ mm}^3$ ) with a <sup>137</sup>Cs  $\gamma$  source at 50 V are shown in Fig. 6. The pulse decay is not exponential as normally expected, which indicates a charge de-trapping effect in the CsPbBr<sub>3</sub> detector. The low probability flat distribution up to  $\sim 100 \mu\text{s}$  is attributed to noise in the detector signals. This particular device (detector II) produces a most probable transit time of  $\sim 20 \mu\text{s}$  at 50 V with a <sup>137</sup>Cs  $\gamma$  source. The large current transit time of perovskite detectors poses challenges to typical  $\gamma$ -ray spectroscopy systems in reconstructing distortion-free energy spectra. The first problem occurs in charge collection process using a charge sensitive preamplifier, in which case a significant ballistic deficit would occur as the current transit time is comparable to preamplifier decay constant [36]–[38]. The second issue is seen at the pulse-shaping step, where a significant ballistic deficit is unavoidable due to the longer current transit time compared to the shaping amplifier’s shaping time constants (e.g., as a rule of thumb, ORTEC typically requires a peaking time 2.2 times of rise time of the pre-amplifier).

The current transit time can always be reduced by applying a higher bias voltage (compare Fig. 5(d) at 500 V and Fig. 6(b) at 50 V), but at the risk of an increased noise that may lead to an even worse spectral performance. Admittedly, a correct selection of suitable hardware could prevent or solve the problem of the ballistic deficit. DPP algorithm, however, offers an alternative low-cost and versatile way to circumvent the issue by dealing with waveforms digitally, hence eliminating the limits of hardware in pulse shaping processes, and then subsequently reconstructing  $\gamma$ -ray energy spectra free of ballistic deficit [36]–[38]. In this work, the raw waveform signals at post preamplifier are directly digitized by an oscilloscope (Tektronix MSO54) and a digital deconvolution was applied to compensate the ballistic deficit at preamplifier charge collection stage, which yields signals whose amplitudes represent the true collected charge without a deficit. The energy spectrum is then reconstructed by calculating the deconvoluted signal amplitudes directly from the difference between the signal peak and the baseline value. In so doing, the pulse shaping process along with potential ballistic deficit at the pulse shaping stage is completely eliminated.

#### B. DPP Algorithm Validation

The first step is to validate the developed DPP algorithm using a commercial detector with transit time much smaller

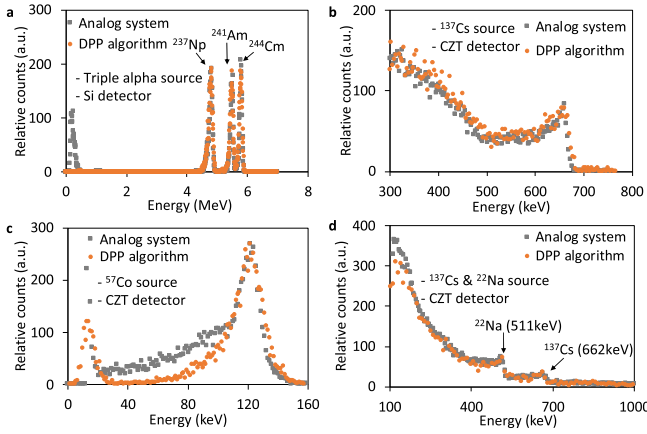


Fig. 7. DPP algorithm validation. (a) Comparison of a triple alpha source energy spectrum of Si detector acquired using the analog spectroscopy system to that reconstructed by the DPP algorithm. (b) Comparison of  $^{137}\text{Cs}$   $\gamma$ -ray energy spectrum of CZT detector acquired using the analog spectroscopy system to that reconstructed by the DPP algorithm. (c) Comparison of  $^{57}\text{Co}$   $\gamma$ -ray energy spectrum of CZT detector acquired using the analog spectroscopy system to that reconstructed by the DPP algorithm. (d) Comparison of  $^{137}\text{Cs}$  and  $^{22}\text{Na}$  (present at the same time)  $\gamma$ -ray energy spectrum of CZT detector acquired using the analog spectroscopy system to that reconstructed by the DPP algorithm.

than the preamplifier's decay constant. In Fig. 7, the energy spectra of  $\gamma$ -ray and alpha-particle sources from commercial-off-the-shelf Si and CZT detectors acquired using the analog spectroscopy system and those reconstructed by the DPP algorithm are compared. The capability of the DPP algorithm to reconstruct energy spectra reliably without distortion is clearly validated by the level of agreement seen between the two types of spectra.

### C. Gamma-Ray Spectra by DPP Algorithm

With the DPP algorithm's capability validated, it is then applied to the reconstruction of distortion-free energy spectra of  $\text{CsPbBr}_3$  detectors with different transit times (see Fig. 8). The spectra acquired using an analog system significantly differs from those reconstructed by the DPP algorithm [see Fig. 8(a) and (b)], when the  $\text{CsPbBr}_3$  detectors (detector II and III) generate signals with an average transit time of  $\sim 20 \mu\text{s}$  (see Fig. 6) while the preamplifier has a decay time of  $50 \mu\text{s}$ . The energy spectra of detector II and III reconstructed by the DPP algorithm show a photopeak, though broadened, which otherwise has been lost in the acquisition by analog spectroscopy system due to significant ballistic deficit. In comparison, as shown in Fig. 8(c) ( $^{137}\text{Cs}$   $\gamma$  source) and Fig. 8(d) ( $^{57}\text{Co}$   $\gamma$  source), the spectra by DPP algorithm agree well with that of an analog system when the average current transit time of the  $\text{CsPbBr}_3$  detector (detector I) is  $\sim 5.8 \mu\text{s}$  [peaked at  $\sim 4 \mu\text{s}$ , in Fig. 5(d)]. Although the ballistic deficit at average transit time  $5.8 \mu\text{s}$  is still possible, it is about one order of magnitude lower than the preamplifier's decay constant ( $50 \mu\text{s}$ ). We conclude that the ballistic deficit does not make a significant impact on spectral performance in this case. It is important to recognize that the transit time is not a constant which depends on charge carrier mobility, applied electric field, and detector thickness. By testing detectors with different transit times, we prove the DPP as a more tolerant and

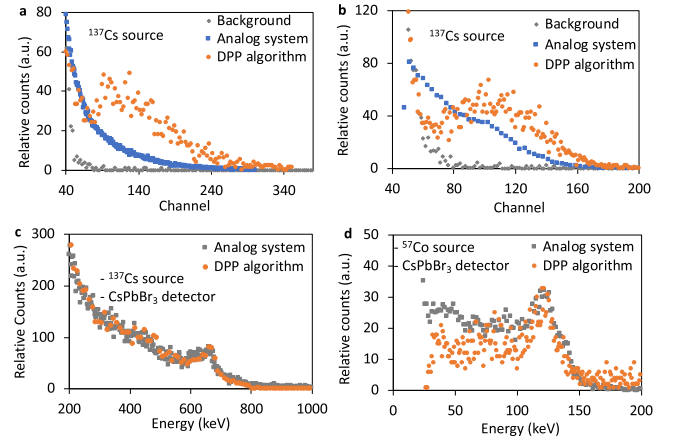


Fig. 8.  $\gamma$ -ray energy spectra of  $\text{CsPbBr}_3$  detectors with different current transit times acquired using the analog spectroscopy system and reconstructed by the DPP algorithm. (a) Comparison of  $^{137}\text{Cs}$   $\gamma$ -ray energy spectrum of  $\text{CsPbBr}_3$  detector II ( $2.3 \times 5.54 \times 6.21 \text{ mm}^3$ ) with current transit time of  $\sim 20 \mu\text{s}$  at  $50 \text{ V}$  (see Fig. 6). (b) Comparison of  $^{137}\text{Cs}$   $\gamma$ -ray energy spectrum of  $\text{CsPbBr}_3$  detector III ( $3 \times 7.35 \times 7.35 \text{ mm}^3$ ) with current transit time of  $\sim 20 \mu\text{s}$  at  $600 \text{ V}$ . (c) Comparison of  $^{137}\text{Cs}$   $\gamma$ -ray energy spectrum of  $\text{CsPbBr}_3$  detector I ( $2.53 \times 7.08 \times 8.29 \text{ mm}^3$ ) with current transit time of  $\sim 5.8 \mu\text{s}$  at  $500 \text{ V}$  [see Fig. 5(d)]. (d) Comparison of  $^{57}\text{Co}$   $\gamma$ -ray energy spectrum of  $\text{CsPbBr}_3$  detector I ( $2.53 \times 7.08 \times 8.29 \text{ mm}^3$ ) with current transit time of  $\sim 5.8 \mu\text{s}$  at  $500 \text{ V}$  [see Fig. 5(d)].

versatile way of producing energy spectrum, with resolution similar to or even better than those acquired by an analog system.

## IV. CONCLUSION

In this work, we measured and evaluated the  $\gamma$ -ray spectra of  $^{137}\text{Cs}$ ,  $^{57}\text{Co}$ , and  $^{241}\text{Am}$  sources from the  $\text{CsPbBr}_3$  detector with 5.5% FWHM at 662 keV, 13.1% FWHM at 122 keV, and 28.3% FWHM at 59.5 keV, respectively. Better hole transport properties compared with that of an electron are demonstrated at the spectroscopic level, and the averaged electron-hole  $\mu\tau$  product is evaluated to be  $4.0 \times 10^{-4} \text{ cm}^2\text{V}^{-1}$ , using Hecht equation fit to the CCE versus detector bias plot derived from  $^{137}\text{Cs}$  energy spectra. Electron-hole averaged mobility was estimated to be  $22 \text{ cm}^2\text{V}^{-1}\text{s}^{-1}$ . The slower electron transport manifested itself on the  $\gamma$ -ray spectra as a low-energy tailing, suggesting the improvement of electrode design (e.g., pixelated electrode) for further significant energy resolution improvement. A linear energy response of the  $\text{CsPbBr}_3$  detector is exhibited by fit to the channel versus energy plot with  $R^2 = 0.999982$ . In addition, potential energy spectra distortion due to the long current transit time of perovskite detectors is discussed and methods to eliminate such energy spectrum distortion by means of the DPP algorithm are presented.

## ACKNOWLEDGMENT

The content of the information does not necessarily reflect the position or the policy of the federal government, and no official endorsement should be inferred.

## REFERENCES

- [1] K. Iniewski, "CZT detector technology for medical imaging," *J. Instrum.*, vol. 9, no. 11, Nov. 2014, Art. no. C11001.



- [2] Q. Li *et al.*, "Study of thick CZT detectors for X-ray and gamma-ray astronomy," *Astroparticle Phys.*, vol. 34, no. 10, pp. 769–777, May 2011.
- [3] R. Carchon, M. Moeslinger, L. Bourva, C. Bass, and M. Zendel, "Gamma radiation detectors for safeguards applications," *Nucl. Instrum. Methods Phys. Res. A, Accel., Spectrometers, Detect. Assoc. Equip.*, vol. 579, no. 1, pp. 380–383, Aug. 2007.
- [4] F. Zhang, C. Herman, Z. He, G. De Geronimo, E. Vernon, and J. Fried, "Characterization of the H3D ASIC readout system and 6.0 cm<sup>3</sup> 3-D position sensitive CdZnTe detectors," *IEEE Trans. Nucl. Sci.*, vol. 59, no. 1, pp. 236–242, Feb. 2012.
- [5] U. Roy, S. Weiler, and J. Stein, "Growth and interface study of 2 in diameter CdZnTe by THM technique," *J. Cryst. Growth*, vol. 312, no. 19, pp. 2840–2845, Sep. 2010.
- [6] V. Carcelén *et al.*, "Influence of thermal environments on the growth of bulk cadmium zinc telluride (CZT) single crystals," *J. Cryst. Growth*, vol. 311, no. 5, pp. 1264–1267, Feb. 2009.
- [7] A. E. Bolotnikov *et al.*, "Large area/volume CZT nuclear detectors," *Phys. Status Solidi C*, vol. 2, no. 5, pp. 1495–1503, 2005.
- [8] H. Wei *et al.*, "Dopant compensation in alloyed CH<sub>3</sub>NH<sub>3</sub>PbBr<sub>3-x</sub>Cl<sub>x</sub> perovskite single crystals for gamma-ray spectroscopy," *Nature Mater.*, vol. 16, no. 8, pp. 826–833, Aug. 2017.
- [9] H. Wei *et al.*, "Halide lead perovskites for ionizing radiation detection," *Nature Commun.*, vol. 10, no. 1, p. 1066, 2019.
- [10] D. Shi *et al.*, "Low trap-state density and long carrier diffusion in organolead trihalide perovskite single crystals," *Science*, vol. 347, no. 6221, pp. 519–522, Jan. 2015.
- [11] X. Wen *et al.*, "Defect trapping states and charge carrier recombination in organic-inorganic halide perovskites," *J. Mater. Chem. C*, vol. 4, no. 4, pp. 793–800, Dec. 2015.
- [12] X. Zheng *et al.*, "Defect passivation in hybrid perovskite solar cells using quaternary ammonium halide anions and cations," *Nature Energy*, vol. 2, no. 7, 2017, Art. no. 17102.
- [13] J. Kang and L.-W. Wang, "High defect tolerance in lead halide perovskite CsPbBr<sub>3</sub>," *J. Phys. Chem. Lett.*, vol. 8, no. 2, pp. 489–493, Jan. 2017.
- [14] R. J. Sutton *et al.*, "Bandgap-tunable cesium lead halide perovskites with high thermal stability for efficient solar cells," *Adv. Energy Mater.*, vol. 6, no. 8, Apr. 2016, Art. no. 1502458.
- [15] S. Yakunin *et al.*, "Detection of gamma photons using solution-grown single crystals of hybrid lead halide perovskites," *Nature Photon.*, vol. 10, no. 9, pp. 585–589, Sep. 2016.
- [16] S. Yang, Z. Xu, S. Xue, P. Kandlakunta, L. Cao, and J. Huang, "Organohalide lead perovskites: More stable than glass under gamma-ray radiation," *Adv. Mater.*, vol. 31, no. 4, Jan. 2019, Art. no. 1805547.
- [17] Y. He *et al.*, "Resolving the energy of  $\gamma$ -ray photons with MAPbI<sub>3</sub> single crystals," *ACS Photon.*, vol. 5, no. 10, pp. 4132–4138, Oct. 2018.
- [18] B. Conings *et al.*, "Intrinsic thermal instability of methylammonium lead trihalide perovskite," *Adv. Energy Mater.*, vol. 5, no. 15, Aug. 2015, Art. no. 1500477.
- [19] A. H. Slavney, R. W. Smaha, I. C. Smith, A. Jaffe, D. Umeyama, and H. I. Karunadasa, "Chemical approaches to addressing the instability and toxicity of lead-halide perovskite absorbers," *Inorg. Chem.*, vol. 56, no. 1, pp. 46–55, Jan. 2017.
- [20] T. Leijtens, G. E. Eperon, N. K. Noel, S. N. Habisreutinger, A. Petrozza, and H. J. Snaith, "Stability of metal halide perovskite solar cells," *Adv. Energy Mater.*, vol. 5, no. 20, Oct. 2015, Art. no. 1500963.
- [21] D. N. Dirin, I. Cherniukh, S. Yakunin, Y. Shynkarenko, and M. V. Kovalenko, "Solution-grown CsPbBr<sub>3</sub> perovskite single crystals for photon detection," *Chem. Mater.*, vol. 28, no. 23, pp. 8470–8474, Dec. 2016.
- [22] C. C. Stoumpos *et al.*, "Crystal growth of the perovskite semiconductor CsPbBr<sub>3</sub>: A new material for high-energy radiation detection," *Cryst. Growth Des.*, vol. 13, no. 7, pp. 2722–2727, Jul. 2013.
- [23] J. Ding, S. Du, Z. Zuo, Y. Zhao, H. Cui, and X. Zhan, "High detectivity and rapid response in perovskite CsPbBr<sub>3</sub> single-crystal photodetector," *J. Phys. Chem. C*, vol. 121, no. 9, pp. 4917–4923, Mar. 2017.
- [24] Y. Rakita *et al.*, "Low-temperature solution-grown CsPbBr<sub>3</sub> single crystals and their characterization," *Cryst. Growth Des.*, vol. 16, no. 10, pp. 5717–5725, Oct. 2016.
- [25] J.-H. Cha *et al.*, "Photoresponse of CsPbBr<sub>3</sub> and Cs<sub>4</sub>PbBr<sub>6</sub> perovskite single crystals," *J. Phys. Chem. Lett.*, vol. 8, no. 3, pp. 565–570, Feb. 2017.
- [26] Y. He *et al.*, "High spectral resolution of gamma-rays at room temperature by perovskite CsPbBr<sub>3</sub> single crystals," *Nature Commun.*, vol. 9, no. 1, p. 1609, 2018.
- [27] A. Ruben *et al.*, "A new, versatile, high-performance digital pulse processor with application to neutron/gamma-ray pulse-shape discrimination in scintillator detectors," in *Proc. Nima\_Sorma XVII*, 2018.
- [28] E. Lukosi *et al.*, "Methylammonium lead tribromide semiconductors: Ionizing radiation detection and electronic properties," *Nucl. Instrum. Methods Phys. Res. A, Accel., Spectrometers, Detect. Associated Equip.*, vol. 927, pp. 401–406, May 2019.
- [29] J. Fink, H. Krüger, P. Lodomez, and N. Wermes, "Characterization of charge collection in CdTe and CZT using the transient current technique," *Nucl. Instrum. Methods Phys. Res. A, Accel., Spectrometers, Detect. Associated Equip.*, vol. 560, no. 2, pp. 435–443, May 2006.
- [30] Y. He *et al.*, "Perovskite CsPbBr<sub>3</sub> single crystal detector for alpha-particle spectroscopy," *Nucl. Instruments Methods Phys. Res. A, Accel., Spectrometers, Detect. Associated Equip.*, vol. 922, pp. 217–221, Apr. 2019.
- [31] A. Shor, Y. Eisen, and I. Mardor, "Optimum spectroscopic performance from CZT  $\gamma$ - and X-ray detectors with pad and strip segmentation," *Nucl. Instrum. Methods Phys. Res. A, Accel., Spectrometers, Detect. Associated Equip.*, vol. 428, no. 1, pp. 182–192, Jun. 1999.
- [32] Z. He, "Review of the Shockley–Ramo theorem and its application in semiconductor gamma-ray detectors," *Nucl. Instrum. Methods Phys. Res. A, Accel., Spectrometers, Detect. Associated Equip.*, vol. 463, nos. 1–2, pp. 250–267, May 2001.
- [33] S. Incerti *et al.*, "The geant4-DNA project," *Int. J. Model. Simul. Sci. Comput.*, vol. 1, no. 2, pp. 157–178, Jun. 2010.
- [34] R. Devanathan *et al.*, "Signal variance in gamma-ray detectors—A review," *Nucl. Instrum. Methods Phys. Res. A, Accel., Spectrometers, Detect. Associated Equip.*, vol. 565, no. 2, pp. 637–649, 2006.
- [35] Z. W. Bell *et al.*, "Neutron detection with LiInSe<sub>2</sub>," in *Proc. Hard X-Ray, Gamma-Ray, Neutron Detector Phys. XVII*, Aug. 2015, Art. no. 95930D.
- [36] V. T. Jordanov, "Unfolding-synthesis technique for digital pulse processing. Part 1: Unfolding," *Nucl. Instrum. Methods Phys. Res. A, Accel., Spectrometers, Detect. Associated Equip.*, vol. 805, pp. 63–71, Jan. 2016.
- [37] S. Saxena *et al.*, "Digital pulse deconvolution with adaptive shaping for real-time high-resolution high-throughput gamma spectroscopy," *Nucl. Instrum. Methods Phys. Res. A, Accel., Spectrometers, Detect. Associated Equip.*, to be published.
- [38] A. Georgiev and W. Gast, "Digital pulse processing in high resolution, high throughput, gamma-ray spectroscopy," *IEEE Trans. Nucl. Sci.*, vol. 40, no. 4, pp. 770–779, Aug. 1993.